STARS

Electronic Theses and Dissertations, 2020-

2020

Contact Mechanics of Fish Scale Inspired Exoskeletal Components on a Nonlinear Elastic Substrate

Jeremy Stephen
University of Central Florida

Part of the Mechanical Engineering Commons

Find similar works at: https://stars.library.ucf.edu/etd2020

University of Central Florida Libraries http://library.ucf.edu

University of Central Florida

STARS
Showcase of Text, Archives, Research & Scholarship

CONTACT MECHANICS OF FISH SCALE INSPIRED EXOSKELETAL
COMPONENTS ON A NONLINEAR ELASTIC SUBSTRATE

by

JEREMY LLOYD STEPHEN
B.S. University of Central Florida, 2019

A thesis submitted in partial fulfillment of the requirements
for the degree of Master of Science
in the Department of Mechanical and Aerospace Engineering
in the College of Engineering and Computer Science
at the University of Central Florida
Orlando, Florida

Spring Term
2020

Major Professor: Ranajay Ghosh

ABSTRACT

The contact mechanics of structures with exoskeletal components deviate significantly from classical Hertzian and non-linear models. In the case of fish scale inspired samples under blunt indentation loading these factors are inherently tied to both the size of the indenter and the scales' distribution and orientation. Control of these geometric parameters provides a pathway to tailor the properties of surfaces for better grip, damage mitigation and controlled deformation. This study explores the response of a substrate with stiff scales protruding from its surface, which is comprised of a soft elastomeric material with properties typical of those in soft robotics applications. It is found that the exoskeletal components amplify the nonlinearly of the system by artificially increasing the effective Hertzian contact area, which alters the contact stiffness and breaks the symmetry of the load across the surface. These effects are quantified using a combination of numerical modeling, finite element (FE) computation and experimental 3D Digital Image Correlation (DIC). While previous works have focused on biological fish scales, fully embedded scale composites and perforation studies, this study investigates and develops a numerical model to quantify the contact behavior of nonlinear elastic substates with exoskeletal scale structures.

ACKNOWLEDGEMENTS

TABLE OF CONTENTS

LIST OF FIGURES

LIST OF TABLES

CHAPTER 1: INTRODUCTION

1.1 Scales as a Biomimetic Material

Early fish began developing dermal armor at the beginning of the Paleozoic period as protection from predators (Bruet, Song, Boyce, & Ortiz, 2008). Over the course of 500 million years, these ancient fish armors evolved into a new form of protection consisting of small overlapping armored plates with decreased weight and improved flexibility, balancing protection and maneuverability (Bruet, Song, Boyce, & Ortiz, 2008; Ehrlich, 2015). These scale systems combined surface hardness with tuned anisotropic flexibility (Browning, Ortiz, & Boyce, 2013), allowing maneuverability while stiffening at high curvatures (Martini & Barthelat, 2016) and providing puncture resistance (Vernerey, Musiket, & Barthelat, 2013; Funk, et al., 2015; Zhu, Barthelat, & Vernerey, 2013; Porter, Ravikumar, Barthelat, & Martini, 2017; Chintapalli, Mirkhalaf, Dastjerdi, & Barthelat, 2014), as shown in Figure 1.
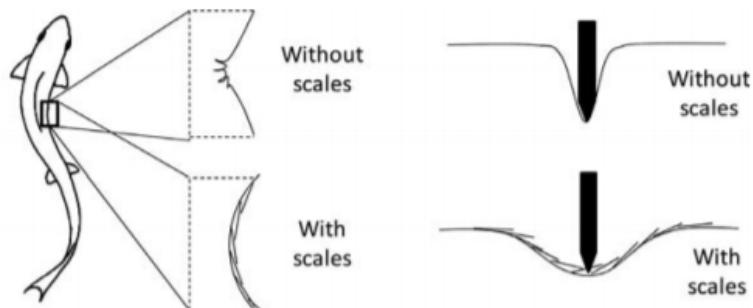
Figure 1. The role of fish scales under deformation, (Zhu, Barthelat, & Vernerey, 2013)

Various species of fish also have scale shapes and articulation patterns that result in functions beyond defense, including drag reduction and anti-biofouling effects (Porter, Ravikumar, Barthelat, & Martini, 2017). However, one trait that remains constant is that the scales are several

orders of magnitude stiffer than their substrates (Funk, et al., 2015; Martini & Barthelat, 2016; Chintapalli, Mirkhalaf, Dastjerdi, & Barthelat, 2014) in order to provide adequate protection.

Due to their clear advantages, these scale structures are ideal biomimetic materials. Biomimetics, or the synthetic imitation of biological systems, is a field which utilizes the unique features of highly optimized structures that have survived the test of time through evolution to develop efficient engineering materials (Zhu, Barthelat, & Vernerey, 2013). Some notable examples in modern biomimicry include the adhesive power of gecko foot microstructures (Autumn & Gravish, 2008) and the dynamic camouflage of cephalopods (Hanlon, 2007). However, the protective capabilities of scale structures have been utilized throughout history. Scales are lightweight (Vernerey & Barthelat, 2014), while combining strength, hardness, toughness and flexibility (Funk, et al., 2015), and overlapping scales provide redundancy so that the entire system is not compromised if certain sections are damaged (Funk, et al., 2015; Chintapalli, Mirkhalaf, Dastjerdi, & Barthelat, 2014). They can also reduce weight, transfer load, redistribute stress (Reichert, 2010; Martini, Balit, & Barthelat, 2017) and increase energy dissipation (Reichert, 2010) in armored structures. These properties made the biomimetic development of scale structures integral to the production of improved armors (Murcia, 2017; White, 2018), which were considered a huge milestone in military development (Tsurtsumia, 2011). Some notable examples include armors used by the ancient Persians (Murcia, 2017; Ehrlich, 2015), and the Roman Empire's Lorica Squamata and Lorica Plumata armors (Murcia, 2017; Vernerey & Barthelat, 2014; Ehrlich, 2015; Miranda, Pajares, & Meyers, 2018), shown in Figure 2.

Figure 2. Soldiers in lorica squamata, and fragments of lorica plumata, (Murcia, 2017)

In order to quantify the protective capabilities of these systems, previous works involving fish scales in a quasi-static environment have focused primarily on the failure mechanisms of individual scales (Martini & Barthelat, 2016; Browning, Ortiz, & Boyce, 2013; Martini, Balit, & Barthelat, 2017), and the resistance of fully embedded scale composites to deformation (Browning, Ortiz, & Boyce, 2013; Rudykh & Boyce, 2014; Rudykh, Ortiz, & Boyce, 2015). However, the potential applications of scaled structures are not only limited to protective equipment, and can extend to other areas including actuation (Rudykh & Boyce, 2014) and soft robotic systems (Ali, Ebrahimi, Stephen, Warren, & Ghosh, 2020).

1.2 Applications in Soft Robotics

Soft robotics is a growing field which has vast potential in applications ranging from surgical robots (Majidi, 2018; Trivedi, Rahn, Kier, & Walker, 2008; Laschi, Mazzolai, & Cianchetti, 2016; Kim, Laschi, & Trimmer, 2013) to agroforestry (Chowdhary, Mattia, Krishnan, Soman, & Lovell, 2019). Hard robots are typically very stiff, with joints that allow simple, precise movements in limited degrees of freedom (Trivedi, Rahn, Kier, & Walker, 2008; Majidi, 2018). Conversely, soft

3

robots are made of compliant materials and are capable of far more complex actions than their hard-robotic counterparts, with theoretically infinite degrees of freedom, increasing their adaptability (Trivedi, Rahn, Kier, & Walker, 2008). While these soft robots utilize a wide variety of actuation mechanisms, ranging from pneumatics to shape memory alloys, their complex actions are often derived from the geometric properties of biological systems (Kim, Laschi, & Trimmer, 2013; Laschi, Mazzolai, & Cianchetti, 2016; Pfeifer, Lungarella, & IIda, 2012; Marchese, Onal, & Rus, 2014; Hao, et al., 2017), as shown in Figure 3.
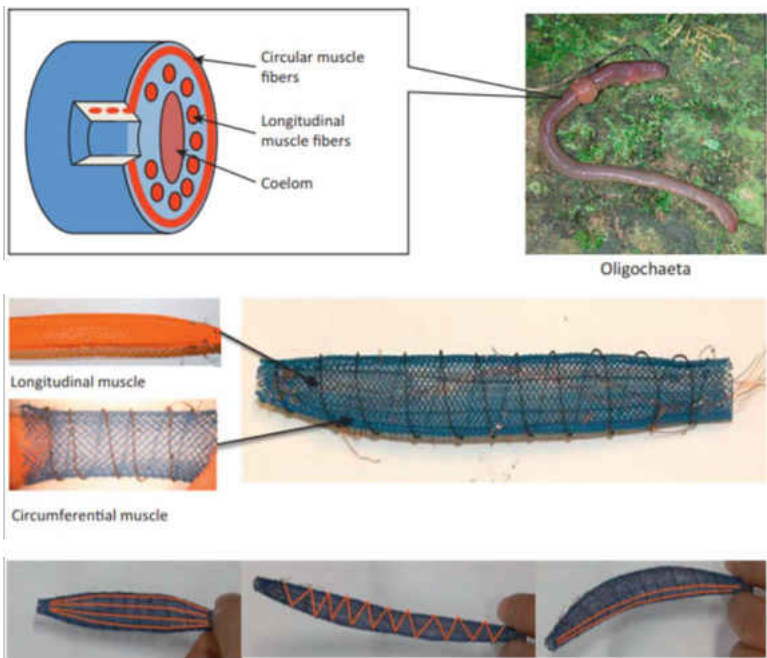
Figure 3. Soft robot inspired by earth worm musculature, (Kim, Laschi, & Trimmer, 2013)

To this end, scale systems are an ideal soft robotic material as they provide flexible anisotropic properties, according to the tunable distribution of the scales, which could be used to direct the system without significantly restricting its range of motion. Several recent studies have explored the interactions between scales in the cases of cantilever and three-point beam bending (Ebrahimi,

4

et al., 2019; Ali, Ebrahimi, & Ghosh, 2019; Ali, Ebrahimi, & Ghosh, 2019; Ali, Ebrahimi, & Ghosh, 2019; Ebrahimi, Ali, & Ghosh, 2020). However, with the application of scales as external structures it becomes necessary to explore the contact mechanics of the scale system under indentation loading.

The objective of this study is to develop a model which captures the nonlinear contact behavior of a nonlinear elastic substrate with an exoskeletal system comprised of stiff scales, noting the effects of the exoskeletal scale components in distributing load across the substrate. The reference configuration for the contact experiments is shown in Figure 4.

Figure 4. Reference configuration for scaled sample with η=1.6

The model performance is assessed experimentally for the primary configurations, and 3D DIC is used in tandem with finite element simulations in ABAQUS to track the distribution of stress and strain across the samples. Finite element simulations are also utilized to explore additional cases.

1.3 Nomenclature

The following terms shown in Table 1 are applied throughout the paper to define the variables and parameters used in the Hertzian and Kao models. Additional terms shown in Table 2 are applied to characterize the contact behavior of the scaled system.

Table 1. Terms used in Hertzian and Kao models

Terms	Descriptions
F	Force
d	Displacement
a	Contact area
R	Cylinder radius
h	Cylinder length
E	Young's modulus
ν	Poisson's ratio
C_d	Material constant
n	Stress exponent for nonlinear elastic materials
k	Contact stiffness

Table 2. Additional terms

Terms	Descriptions
L_s	Total Scale length
l_s	Exposed scale length
l_e	Embedded scale length
t	Scale thickness
δ	Distance between scales
θ	Scale angle
η	Ratio of exposed scale length to the distance between scales

CHAPTER 2: MATERIALS AND METHODS

2.1 Sample Configuration and Materials

The scaled system studied in this paper is comprised of a soft substrate covered in rigid scales. A nonlinear elastomeric material was used for the substrate, to mimic soft robotics applications, while the scales were made from galvanized steel. The substrate made of Dragon Skin 20 was measured to have an elastic modulus of 0.34 MPa, while the scales have an elastic modulus of 200000 MPa, therefore the scales are assumed to undergo negligible deformation and are taken as rigid bodies in the finite element analysis. The substrate material is assumed to be nearly incompressible. The dimensions of the substrate are 210 x 25 x 80 mm, and the dimensions of the scales are 35 x 25 x 1 mm with an exposed scale length of 24 mm. The distribution and orientation of the scales are shown in Figure 5.
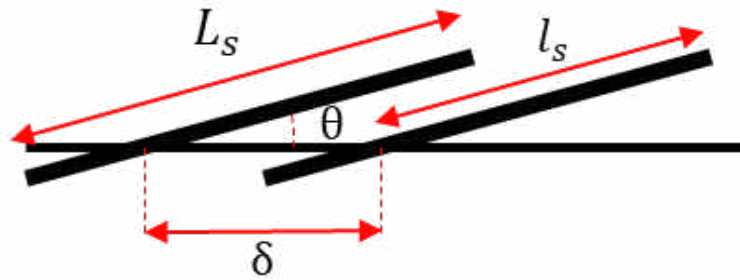
Figure 5. Schematic diagram of scale orientation and distribution

The samples are studied under loading conditions with four different cylindrical indenters with widths of 25 mm and radii of 2.5, 25, 37.5 and 50 mm. These indenters are 3D printed from a resin material with an elastic modulus of 2600 MPa (Formlabs, 2019), and are also taken to be rigid as compared to the substrate.

For each sample the variable η, defined in eq. (1), is varied to show the effects of the scale distribution on the system.

$$\eta = \frac{l_s}{\delta}$$ (1)

For the primary configurations θ is held constant at 10° and η is varied by holding the exposed scale length constant and changing the distance between scales, as shown in Table 3.

Table 3. Primary sample configurations

Configuration	Material	η	l_s	δ	θ
1	Dragon Skin 20	Unscaled	-	-	-
2	Dragon Skin 20	1.2	24	20	10°
3	Dragon Skin 20	1.6	24	15	10°
4	Dragon Skin 20	2.4	24	10	10°

Three additional cases are explored using finite element simulation for a total of five additional configurations using the second primary configuration as a standard, as shown in Table 4. The first additional case varies θ in order to investigate the role of the scale angle in the system response. The second additional case explores the validity of the model for different materials by running simulations for samples made of Dragon Skin 10 and Dragon Skin 30. The third additional case studies the effects of the exposed scale length by varying l_s while holding δ constant.

Table 4. Additional sample configurations

Configuration	Material	η	l_s	δ	θ
5	Dragon Skin 20	1.6	24	15	5°
6	Dragon Skin 10	1.6	24	15	10°
7	Dragon Skin 30	1.6	24	15	10°
8	Dragon Skin 20	1.2	18	15	10°
9	Dragon Skin 20	2.4	36	15	10°

Additionally, material properties in Kao's elastic model are derived for each material considered, as shown in Table 5. For the Dragon Skin 20 material, the elastic modulus, material constant and material exponent are derived experimentally. For additional materials the elastic moduli are given (Smooth-On, Inc.), and the material constants and material exponents are derived from the finite element simulation results.

Table 5. Material properties

Material	E	C_d	n
Dragon Skin 10	0.15	2.58	0.625
Dragon Skin 20	0.34	5.813	0.625
Dragon Skin 30	0.6	10.33	0.625

2.2 Hertzian Contact of Elastic Cylinders

Hertzian contact is originally defined for the contact of two elastic spheres, but can be extended for simple geometries (Popov, 2017). This study looks at the contact of two elastic cylinders with parallel axes. The half width of Hertzian contact area of the two elastic cylinders, which will be referred to simply as the contact area, is given by eq. (2).

$$a = \sqrt{\frac{4FR}{\pi h E^*}} \tag{2}$$

A physical representation of the contact area is given in Figure 6.
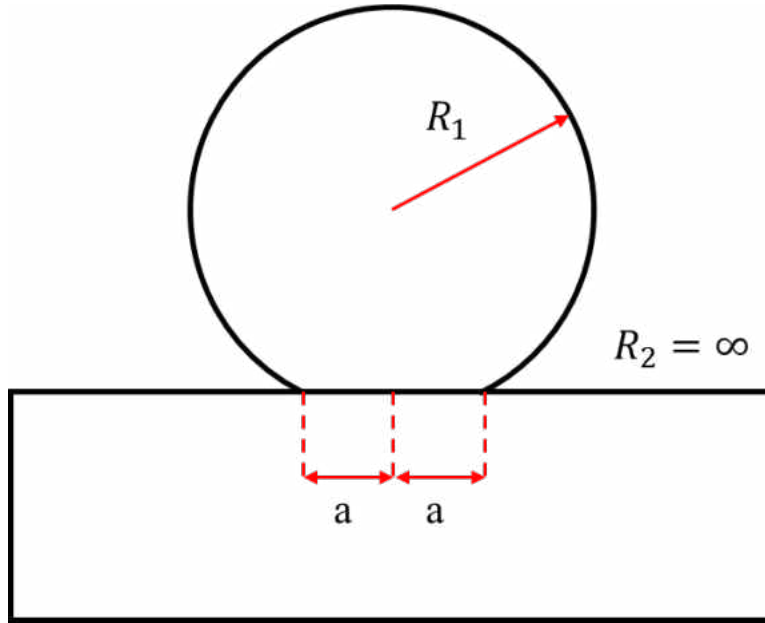
Figure 6. Physical representation of contact area

The parameters E^* and R are functions of the material properties and radii, respectively, of both cylinders, as shown in eq. (3) and (4).

$$\frac{1}{E^*} = \frac{1-v_1^2}{E_1} + \frac{1-v_2^2}{E_2} \qquad (3)$$

$$\frac{1}{R} = \frac{1}{R_1} + \frac{1}{R_2} \qquad (4)$$

The contact of an elastic cylinder with an elastic half-space can be taken as a special case where the radius of the second cylinder is infinity. The contact area is related to the displacement by eq. (5), giving eq. (6) as a linear relation between the force and displacement. The indenter radius drops out of the force-displacement relation for the cylindrical case.

$$d = \frac{a^2}{R} \qquad (5)$$

$$F \approx \frac{\pi}{4} E^* h d \qquad (6)$$

Traditional Hertzian contact assumes frictionless, non-adhesive, linear deformation in the elastic region, with an area of contact much smaller than the relative size of the bodies in contact. Therefore, this theory is insufficient for the case of nonlinear elastic materials undergoing significant deformation.

2.3 Kao's Elastic Model

The elastomeric materials used in soft robotics tend to display nonlinear properties which differ significantly from classical Hertzian contact model. Xydas and Kao developed a nonlinear elastic contact model for soft robotic fingers, which subsumes the Hertzian model, to better define the contact behavior of these materials (Xydas & Kao, 1999; Siciliano & Khatib, 2016). Kao's elastic model is used to define the contact mechanics of soft robotic fingers and originally defines the contact of an elastic sphere with an elastic half plane but, as with the classical Hertzian model, can also be extended for simple geometries. The generalized model can be taken in the form,

$$\frac{F}{A} = c_1 a^{\frac{1}{n}} \tag{7}$$

The parameter A is the total area over which the force is distributed, c_1 is a constant which is related to the indenter radius and nondimensionalized stress components, and n is the stress exponent for nonlinear elastic materials. It should be noted that, contrary to the linear Hertz equation, the force-displacement relation for the nonlinear cylindrical case does depend on the indenter radius, as shown in Figure 7. The total areas for the spherical and cylindrical cases are given as the projection of the indenter shape, shown in eq. (8) and (9) respectively.

$$A_{sphere} = \pi a^2 \tag{8}$$

$$A_{cylinder} = 2ah \tag{9}$$

Taking eq. (7) for the cylindrical case gives

$$F = Ca^{\frac{1}{n}+1} \tag{10}$$

Substituting eq. (5), this takes the form

$$F = C_d d^{\frac{n+1}{2n}} \tag{11}$$
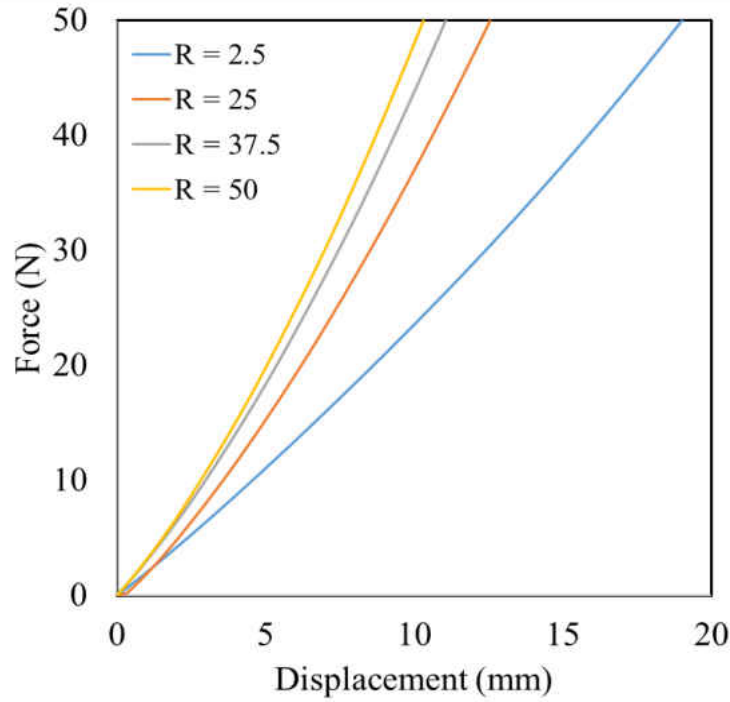
Figure 7. R dependence for an unscaled nonlinear elastic material with E = 0.19 MPa

This relation can be simplified by substituting eq. (12)

$$\zeta = \frac{n+1}{2n} \tag{12}$$

This equation gives the nonlinear force-displacement relationship for nonlinear elastic materials.

$$F = C_d d^{\zeta} \tag{13}$$

Generally, it can be assumed that $0 \leq n \leq 1$, so the exponent in eq. (13) is

12

$$1 \leq \zeta \leq \infty \tag{14}$$

Kao et. al. (Kao & Yang, 2004; Siciliano & Khatib, 2016) also define a contact stiffness k, shown in eq. (15).

$$k = \frac{\partial N}{\partial d} \tag{15}$$

The stiffness is expanded into three forms as functions of the displacement and force, as shown in eq. (16)-(18).

$$k(d) = C_d \zeta d^{\zeta-1} \tag{16}$$

$$k(F) = C_d^{\frac{1}{\zeta}} \zeta F^{\frac{\zeta-1}{\zeta}} \tag{17}$$

$$k(F, d) = \zeta \frac{F}{d} \tag{18}$$

The contact stiffness is plotted as a function of the displacement in Figure 8, below.

Figure 8. Contact stiffness k(d) for Dragon Skin 10, 20 and 30

CHAPTER 3: RESULTS AND DISCUSSION

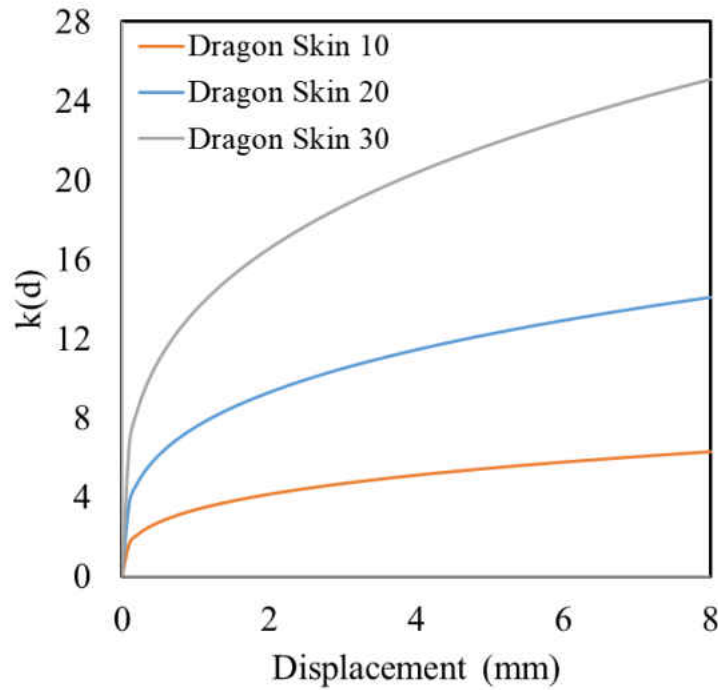## 3.1 Scale Contact Characteristics

The experimental data shows an unexpected behavior in the force-displacement relation for the unscaled and scaled samples in configurations 1-4, as shown in Figure 9. While the scaled samples show a stiffening behavior, there is an unintuitive offset in the response which displays a significantly lower stiffness than that of the unscaled sample. This is found to be due to the interaction between the first scale and the indenter where the embedded portion of the scale resists its rotation, but before the substrate is sufficiently loaded for the system to be dominated by an indentation response. Therefore, the force-displacement relation for the scaled system is divided into two separate regimes: an initial regime dominated by the rotation of the first exposed scale and a second regime dominated by deformation of the substrate material.
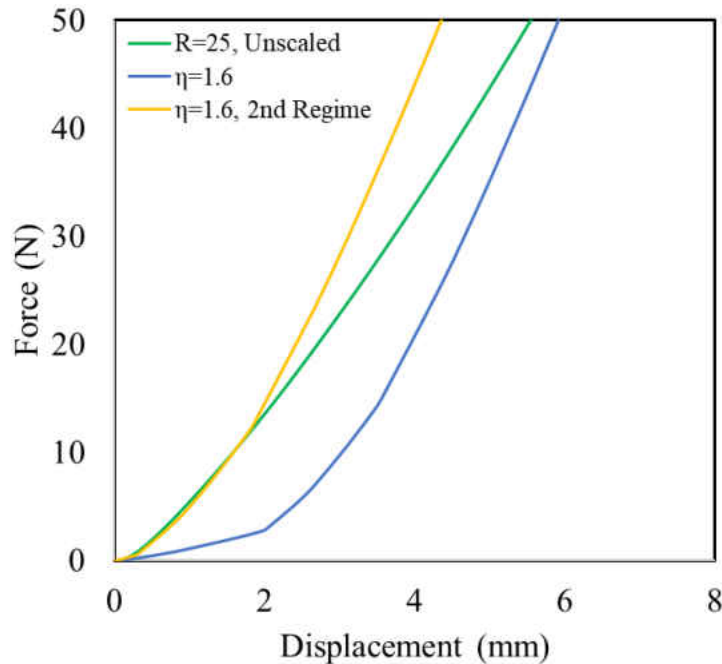
Figure 9. Force-displacement relation for unscaled and η=1.6 configurations

14

For the primary configurations, the length of the first regime is approximated as the point where the first scale contacts the second scale. In Figure 10 it is shown that, at the point of scale contact, the deformation of the substrate material is not significant. The axis of scale rotation is approximated to occur at the midpoint of the embedded scale length, l_e.
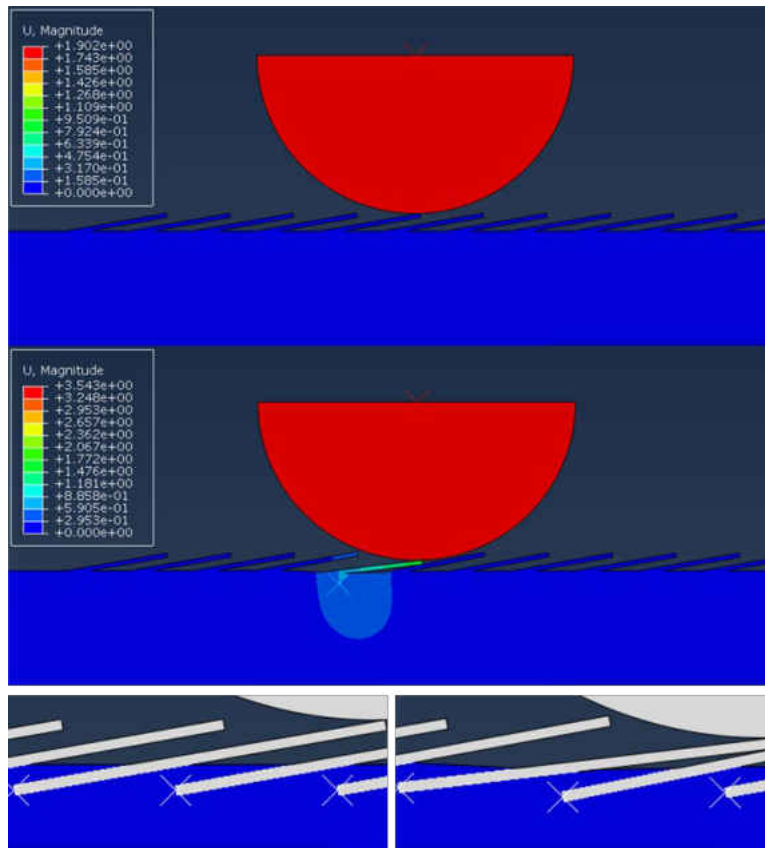
Figure 10. Scale rotation and indentation point

The first regime behavior is dependent on the initial orientation of the scales. Therefore configuration 5 is tested in ABAQUS, to observe the response of a system with a very small θ, where the scales are nearly touching. It is shown that for very small θ the first regime disappears, as expected. However, it also shows a significant stiffening response compared with the reference

15

configuration, as shown in Figure 11. It is observed that this response is due to the decreased θ allowing a greater number of scales to come into contact sooner. Due to the computational cost of simulating configurations with variable θ, further experiments are required to fully explore its role in the system response.
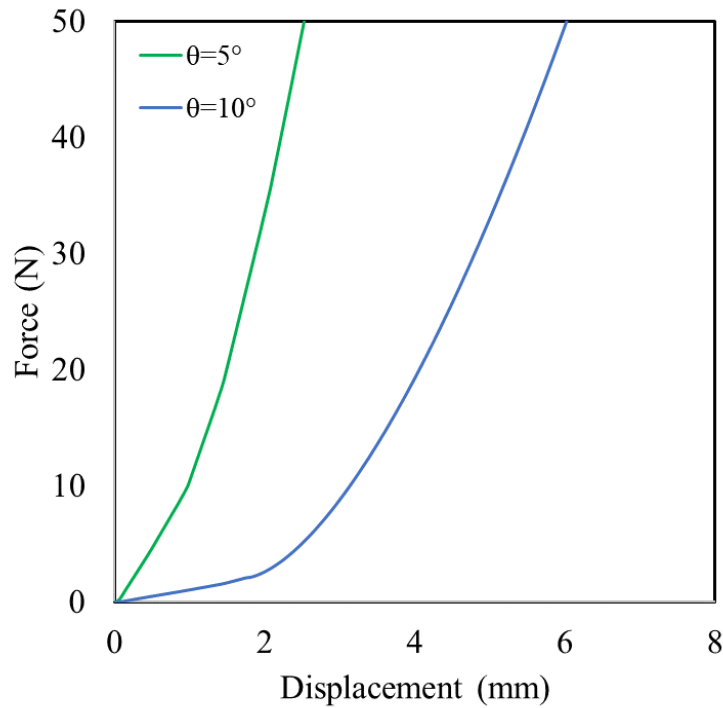
Figure 11. First regime disappears for low θ

It is also notable that the effects of the indenter radius are found to be negligible for the range of indenters tested, as shown in Figure 12. In the unscaled case, the indenter radius affects the system response by altering the contact area. Therefore, it is determined that the contact area is no longer dependent on the indenter radius for the scaled system.
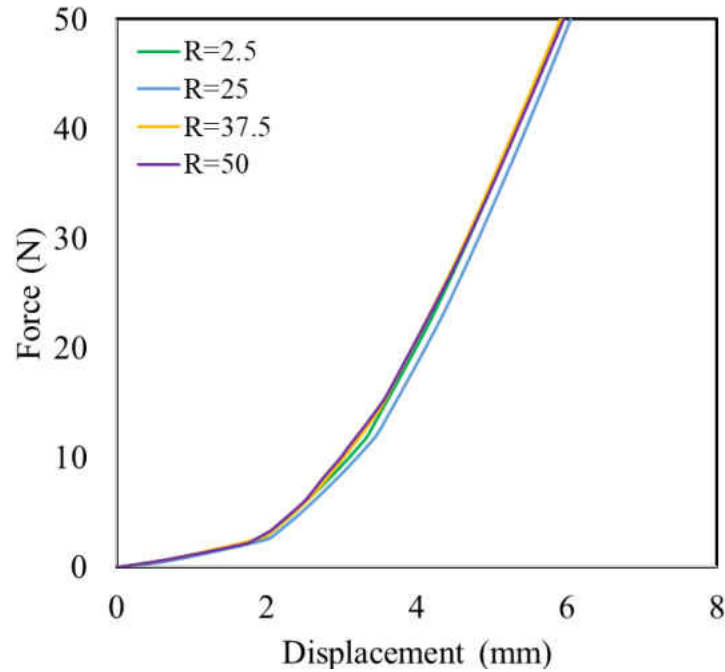
Figure 12. Effects of indenter radius for scaled sample with η=1.6

This study is primarily focused on the quasi-static case; however, a range of test rates are also explored to examine the effects of the scale system together with the rate change properties of the substrate. While this area requires further study, in the initial data it is observed that the nonlinearity of the unscaled response decreases with increasing test rate, where the response becomes more linear as $n \to 1$. Interestingly, the scaled system appears to demonstrate the opposite result, with an increasingly nonlinear response. This suggests that there may be an additional rate dependent mechanism in the scaled system which opposes and overtakes the decrease in nonlinearity of the unscaled material response. The unscaled and scaled responses are plotted below in Figures 13 and 14, respectively. Looking at the logarithmic plots for these respective cases, in Figures 15 and 16, this deviation appears to occur specifically in the early stages of contact. The apparent rate change in the material properties of the unscaled system is shown in Figure 17 and Table 6.
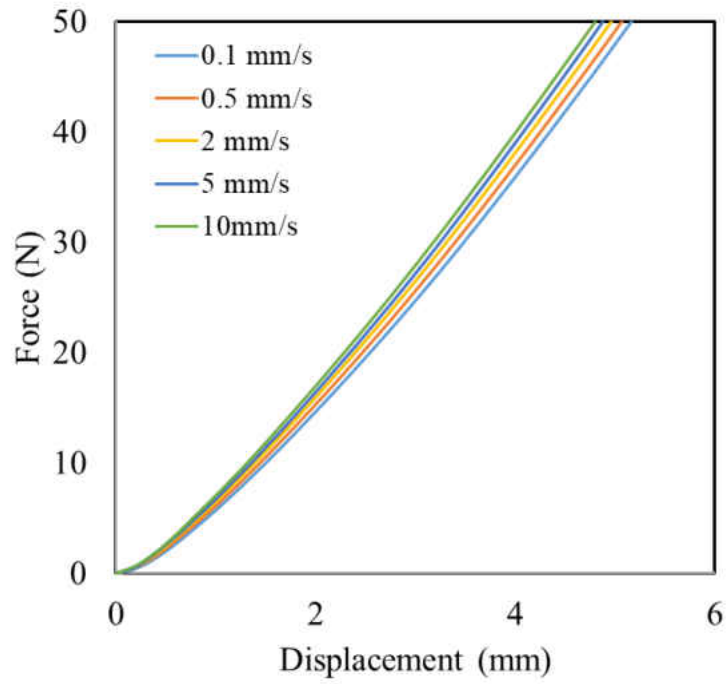
Figure 13. Variable test rate for unscaled configuration
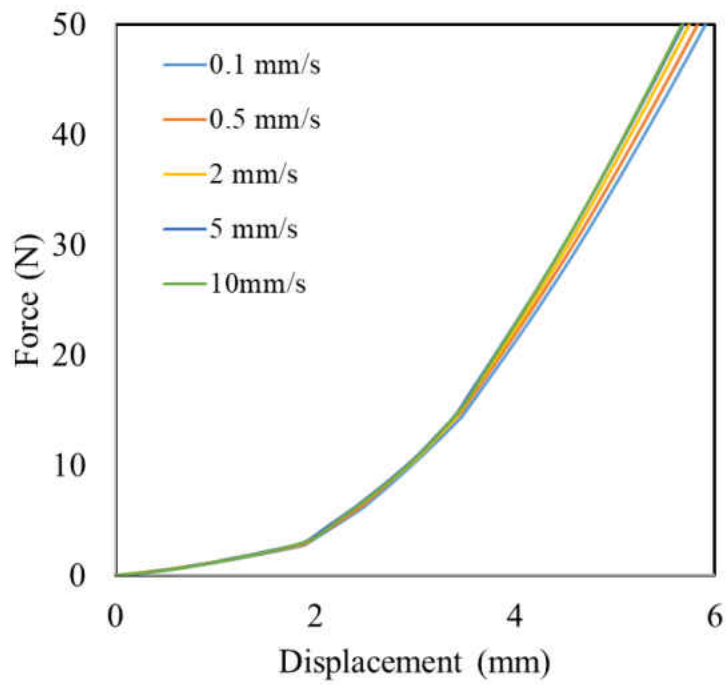
Figure 14. Variable test rate for configuration 3

18
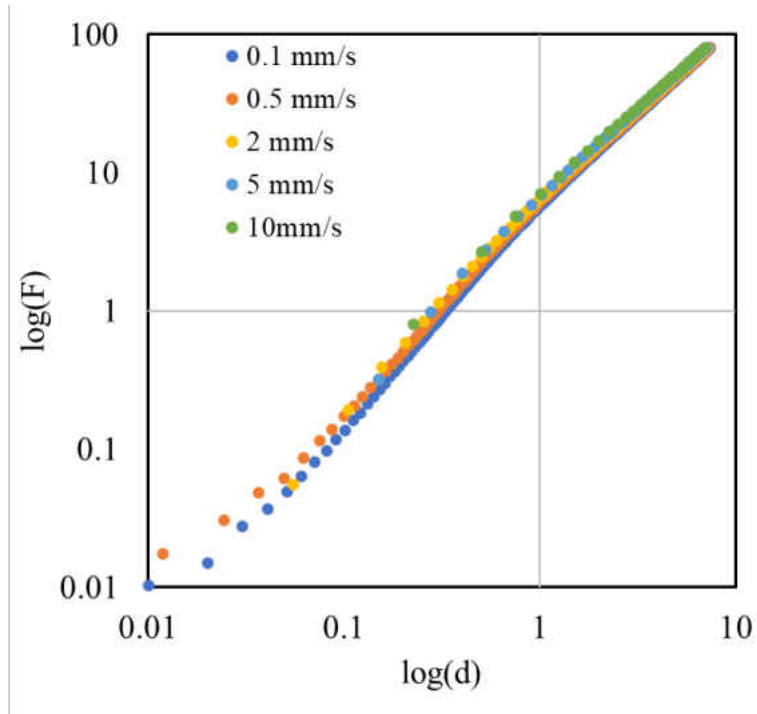
Figure 15. Variable test rate for unscaled configuration, in logarithmic domain
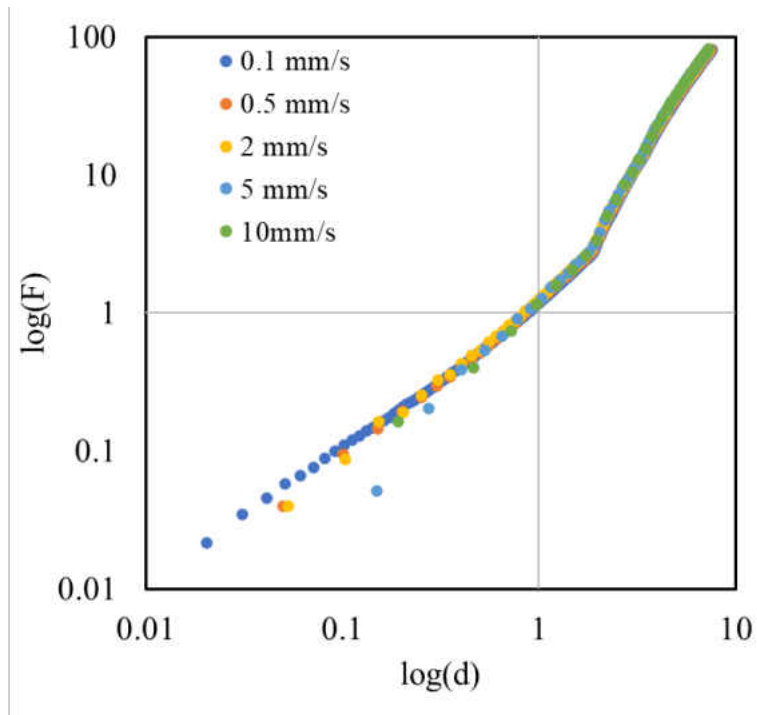
Figure 16. Variable test rate for configuration 3, in logarithmic domain
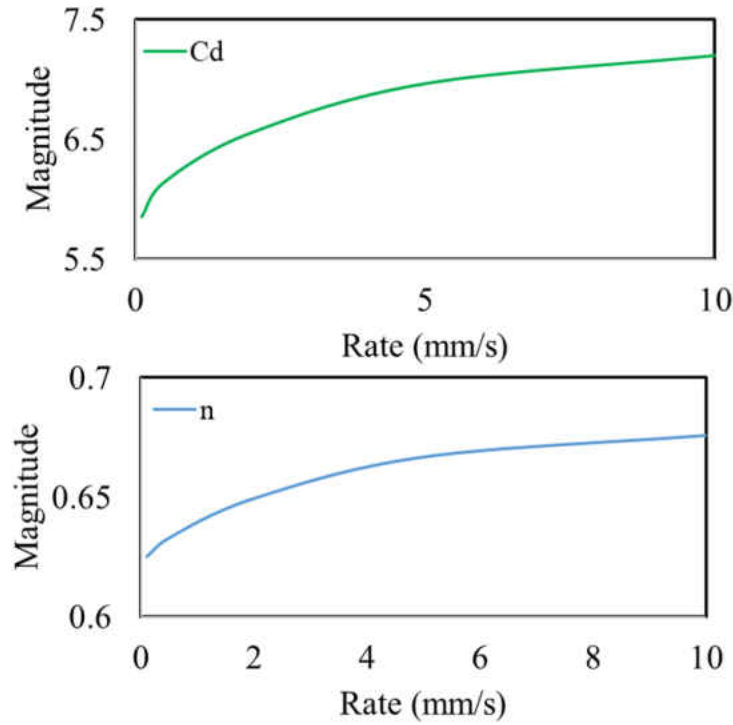
Figure 17. Rate change in material properties for the unscaled configuration

Table 6. Rate change in material properties of unscaled Dragon Skin 20

Rate (mm/s)	C_d	n
0.1	5.813	0.625
0.5	6.104	0.633
2	6.511	0.649
5	6.918	0.667
10	7.15	0.676

3.2 First Regime of Scale Contact

The first regime of scale contact is estimated to extend to the point where the first scale contacts the second scale for the primary configurations. This displacement d_{r1} is demonstrated to be dependent on δ, l_s and L_s, and independent of the material stiffness. Increasing δ lengthens d_{r1} by requiring the scales to rotate further before coming into contact, as shown in Figure 18. Conversely,

20

increasing the ratio of exposed scale length to total scale length is shown to decrease d_{r1}, as there is less distance for the scales to rotate before the substrate begins to significantly deform.
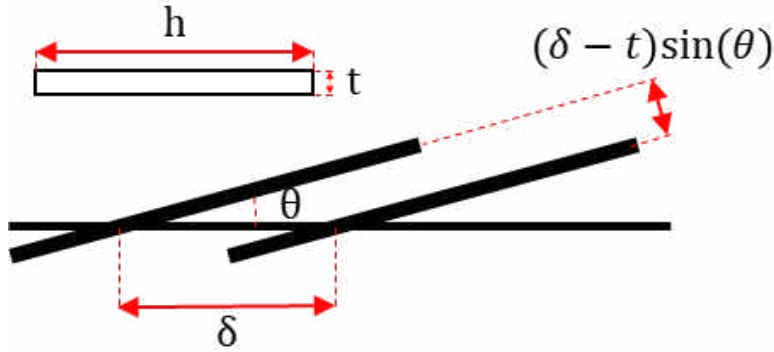
Figure 18. Scale cross section and distance between scales

Analyzing the data from the primary and additional configurations, d_{r1} can be roughly approximated by eq. (19).

$$d_{r1} = \frac{11}{20}\left(\frac{L_s}{l_s}\right)^{0.7}(\delta - t)\sin(\theta) \tag{19}$$

Where the aforementioned relations are expressed by equations (20) and (21).

$$d_{r1} \propto (\delta - t)\sin(\theta) \tag{20}$$

$$d_{r1} \propto \left(\frac{L_s}{l_s}\right)^{0.7} \tag{21}$$

The force-displacement relation for the first regime can be roughly approximated by the equation for a torsional spring, shown in eq. (22), where T is the torque, κ is the rotational spring constant and θ_T is the angle the scale rotates through.

$$T = \kappa\theta_T \tag{22}$$

The torque T is given by eq. (23), where l_r is the rotational length, shown in eq. (24).

$$T = Fl_r \tag{23}$$

$$l_r = l_s + \frac{l_e}{2} \tag{24}$$

The angle θ_T, shown in eq. (25) is dependent on the displacement and rotational length.

$$\theta_T = sin^{-1}\left(\frac{d}{l_r}\right) \tag{25}$$

The spring constant is dependent on δ, the embedded scale length, and the nonlinear stiffness, which is proportional to $d^{\zeta-1}$. Decreasing δ increases the composite density in the embedded portion of the sample resulting in greater subsurface interference which is shown to increase the stiffness in the first regime. Decreasing the ratio of exposed scale length to total scale length is shown to increase the stiffness in the first regime, because there is a greater percentage of the scale that is embedded and resisting the rotation, as shown in Figure 19.
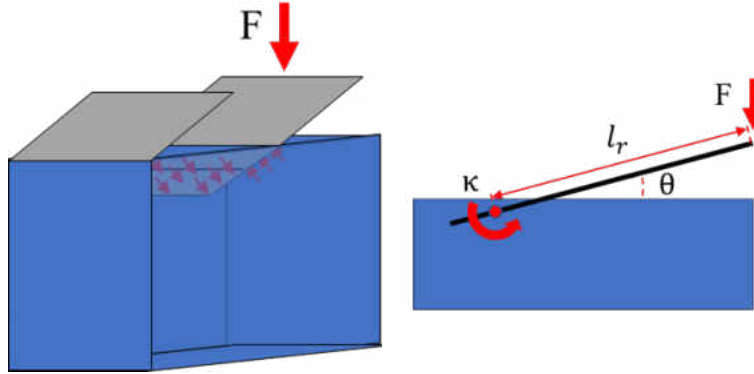
Figure 19. Embedded Scale Interactions

Analyzing the data from the primary and additional configurations, the force-displacement relation is given by eq. (26)

$$F_{r1} = \frac{3}{2}\frac{1}{l_r}El_e^2hd^{\zeta-1}\left(\frac{l_e}{\delta}\right)^{1.5} sin^{-1}\left(\frac{d}{l_r}\right) \tag{26}$$

Where the aforementioned κ dependencies are given by eq. (27) and (28).

$$\kappa \propto \left(Ed^{\zeta-1}\right)(l_e h)\left(\frac{l_e}{2}\right) \qquad (27)$$

$$\kappa \propto \left(\frac{l_e}{\delta}\right)^{1.5} \qquad (28)$$

The model for the first regime is plotted against the experimental data in Figures 20 and 21. It is noted that the configuration with very long exposed scale length, shown in Figure 22, remains in the first regime following contact with the second scale due to the point of contact being far removed from the scale base. This results in a stiffening within the first regime at the point of contact.
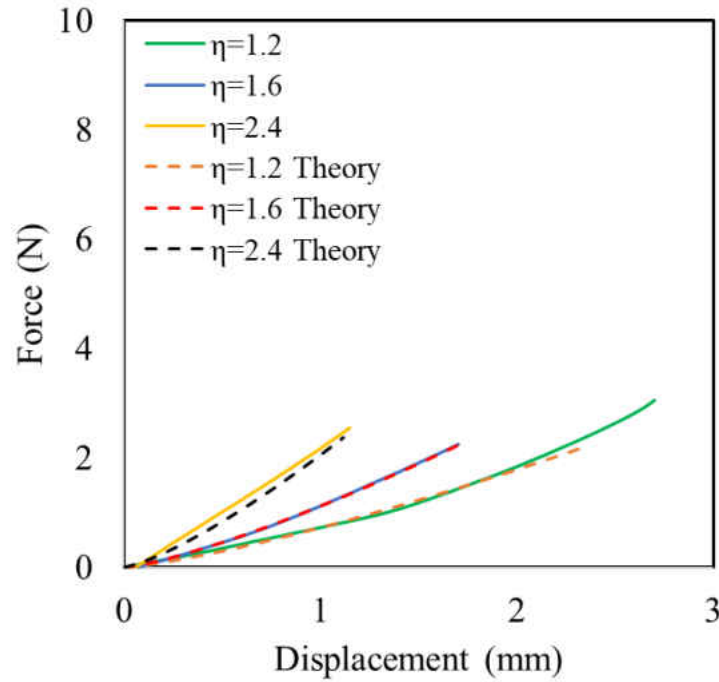
Figure 20. First regime force-displacement relation for varied δ
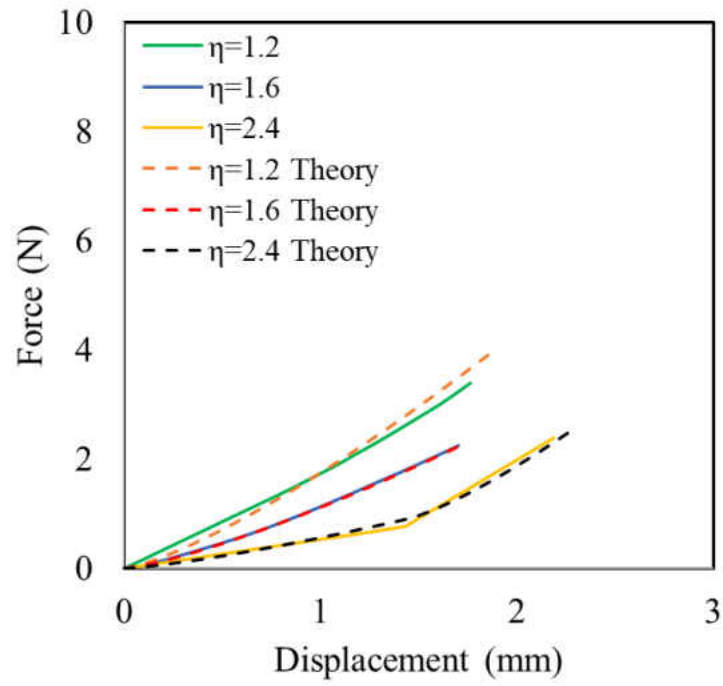
Figure 21. First regime force-displacement relation for varied l_s
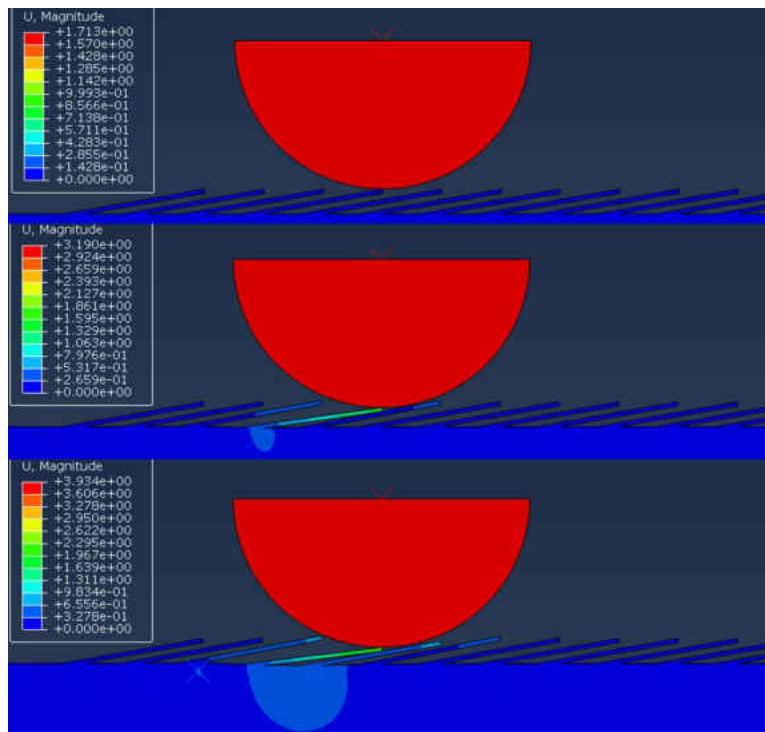
Figure 22. Indentation point for l_s=36 configuration

3.3 Strain Distribution and Contact Area

Finite element simulation is utilized to analyze the strain distribution across the unscaled and scaled configurations, as shown in Figure 23, in order to determine the underlying mechanisms responsible for the system response in the second regime. For a given indentation depth, it is shown that the inclusion of scales causes the strain to be distributed across a greater portion of the sample.
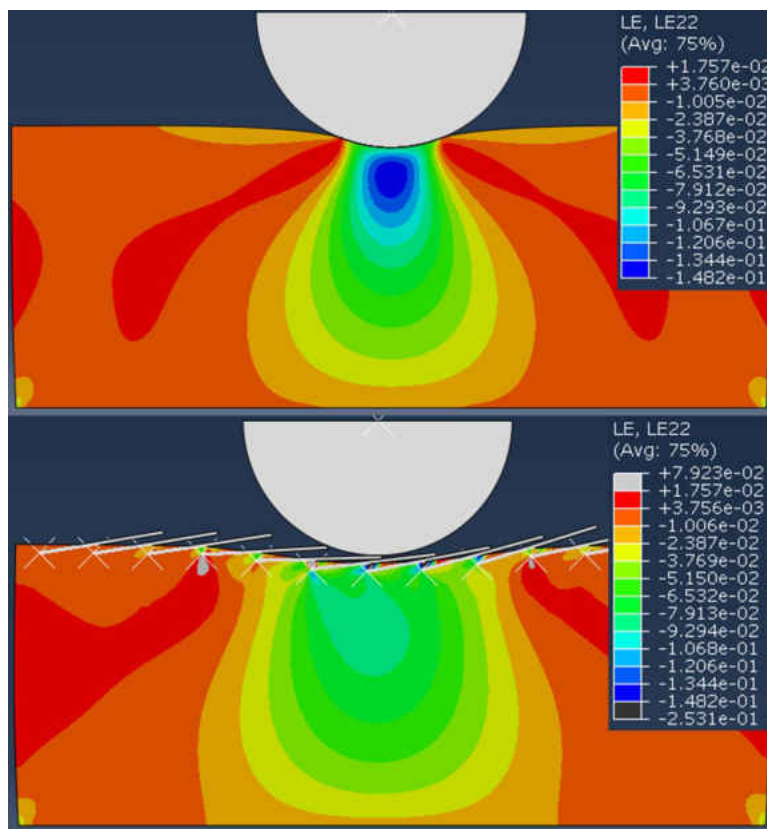
Figure 23. Strain and Strain Energy for plain and scaled samples, shown in ABAQUS

This strain is distributed cleanly from the contact surface for the unscaled configuration. For the scaled configuration, it is shown that the strain stems from the embedded ends of the scales, forming a much rougher surface distribution. Relating this to the unscaled configuration, this is

demonstrated to extend the contact surface beyond the radius of the indenter, as shown in Figure 24. This is observed, in both experimental data and finite element results, to increase both the stiffness and nonlinear response of the system.
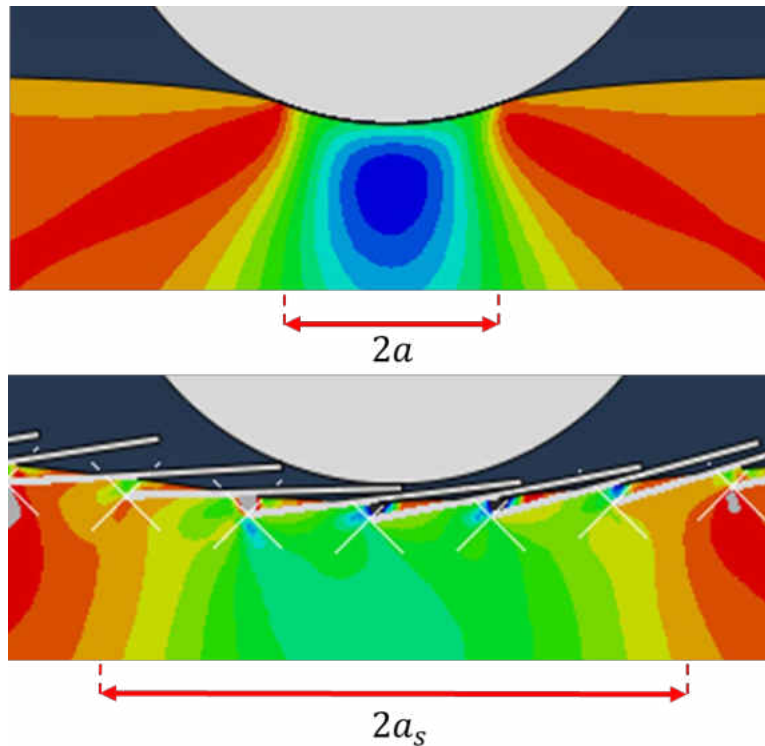
Figure 24. Hertzian vs Effective Scaled contact area, shown in ABAQUS

The primary configurations are also analyzed through digital image correlation, as shown in Figure 25. For a given load, it is observed that increasing η results in a greater distribution throughout the sample, decreasing the magnitude of the strain. This is also observed to coincide with an increase in the surface distribution.
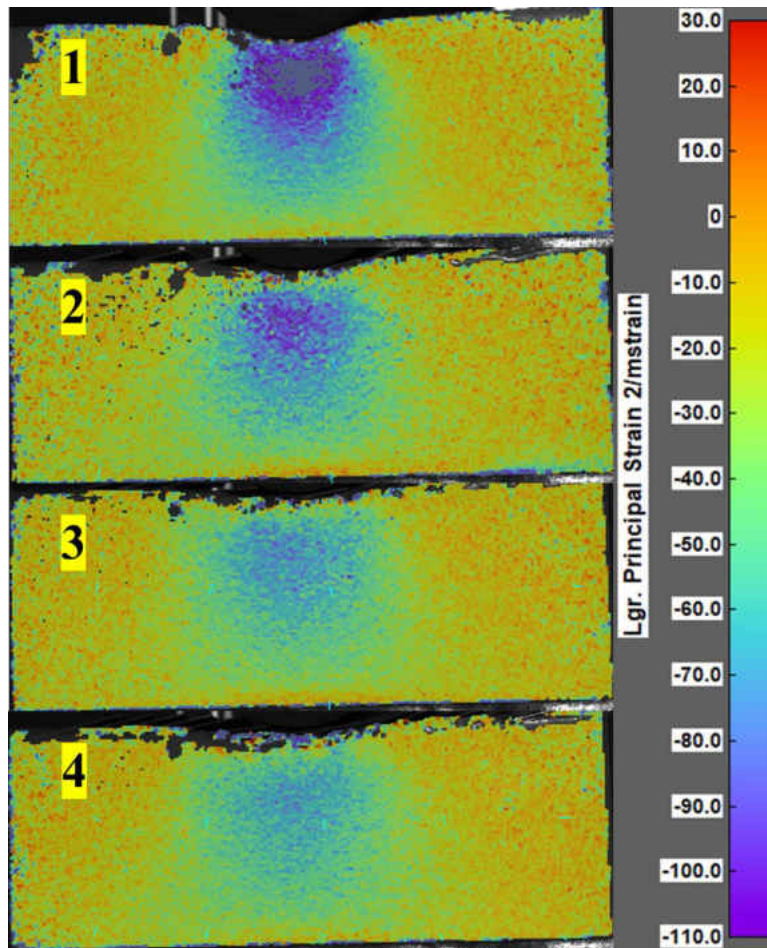
Figure 25. DIC results for primary configurations

These results are compared with the finite element simulations, as shown in Figure 26, and confirm that the strain distribution stems from the embedded ends of the scales and extends beyond the indenter radius at the surface. This is consistent with the previous observation that the system response is not dependent on the indenter radius. From these results, a numerical model is developed to approximate the stiffening response of the second regime of the scaled system as an artificial increase in the effective Hertzian contact area.
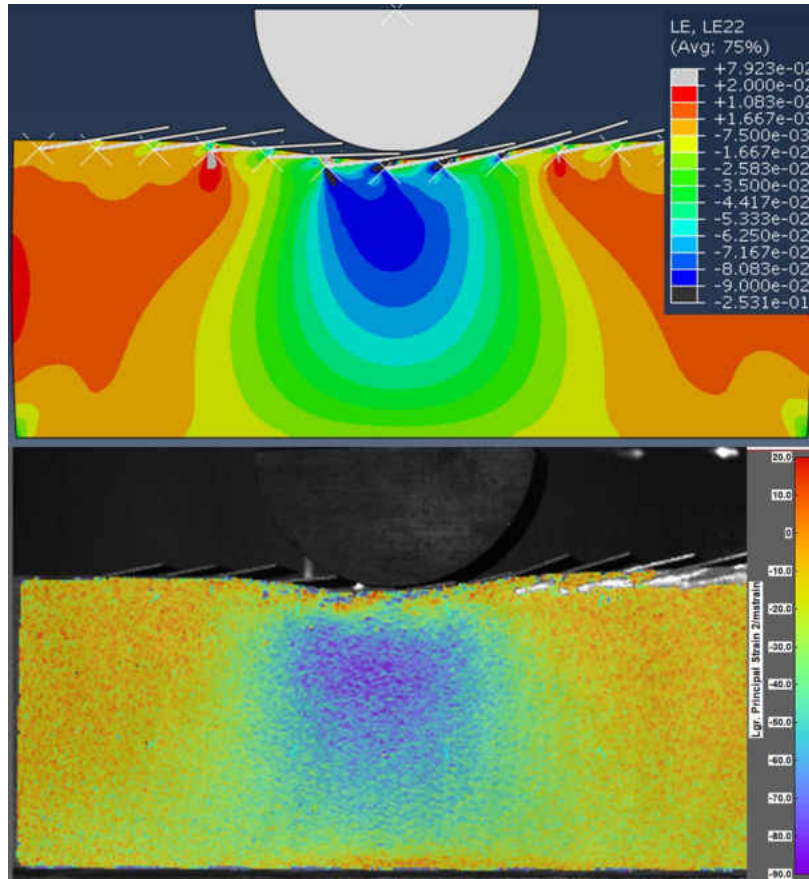
Figure 26. ABAQUS and DIC results for displacement and strain in final stress state

3.4 Second Regime of Scale Contact

The force-displacement relation for the second regime is developed from Kao's elastic model, where eq. (29) is derived from eq. (16) and (18). This separates eq. (13) into linear and nonlinear components which can be represented as an effective nonlinear contact stiffness and a linear displacement.

$$F = (C_d d^{\zeta-1})d \tag{29}$$

The effective contact area and indenter radius for the scaled system are altered by the presence of the exposed scales at the surface of the substrate, as shown in Figure 24. Notably, for the range of

indenters studied, the true indenter radius did not significantly alter the response of the system. Relating the modified parameters to eq. (5), the ratio of the effective displacement to the true displacement is given by eq. (30),

$$\frac{d_s}{d} = \frac{a_s^2 R}{a^2 R_s}$$

(30)

Where d_s, a_s and R_s are the effective displacement, effective contact area and effective indenter radius for the scaled system. This expression can be inserted into eq. (29) to express the effects of the scales as a modifier to the effective contact stiffness, as shown in eq. (31).

$$F_s = C_d \phi^{\zeta-1} d^\zeta$$

(31)

Where ϕ is the stiffening term given by eq. (32).

$$\phi = \frac{a_s^2 R}{a^2 R_s}$$

(32)

From the experimental results, ϕ is determined to be proportional to the displacement and the square root of η, as shown in eq. (33),

$$\phi = \frac{2}{5} \eta^{\frac{1}{2}} d$$

(33)

Which expands eq. (31) to the form given by eq. (34).

$$F_s = C_d \left(\frac{2}{5} \eta^{\frac{1}{2}} \right)^{\zeta-1} d^{2\zeta-1}$$

(34)

The second regime model is plotted with the experimental data in Figure 27. It is shown that the nonlinear stiffening response is fully captured.
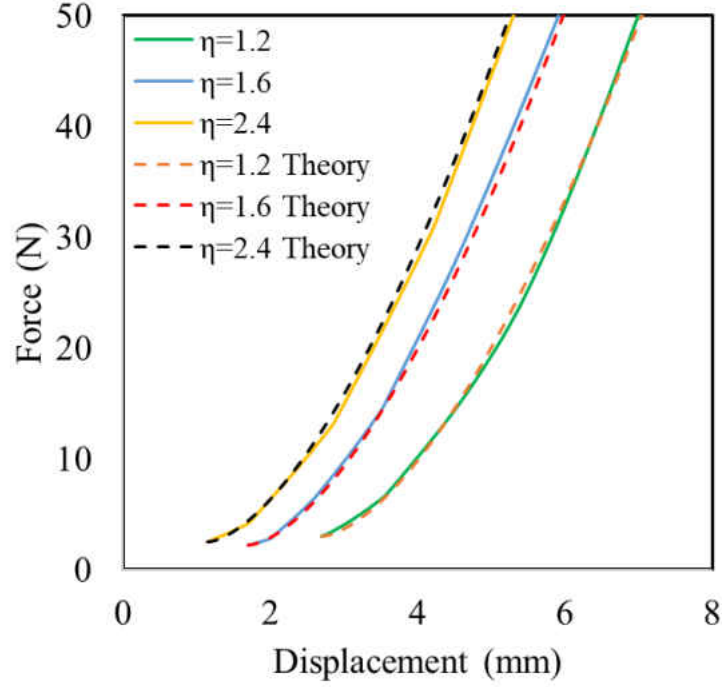
Figure 27. Second regime force-displacement relation

Separating the regimes,

$$F_{r2} = \frac{3}{2}\frac{1}{l_r} E l_e^2 h d_{r1}^{\zeta-1} \left(\frac{l_e}{\delta}\right)^{1.5} sin^{-1}\left(\frac{d_{r1}}{l_r}\right) + C_d \left(\frac{2}{5}\eta^{\frac{1}{2}}\right)^{\zeta-1} (d - d_{r1})^{2\zeta-1} \tag{35}$$

So, the full model takes the form,

$$\begin{cases} F_{r1} = \frac{3}{2}\frac{1}{l_r} E l_e^2 h d^{\zeta-1} \left(\frac{l_e}{\delta}\right)^{1.5} sin^{-1}\left(\frac{d}{l_r}\right) & for\ d \leq d_{r1} \\ F_{r2} = \frac{3}{2}\frac{1}{l_r} E l_e^2 h d_{r1}^{\zeta-1} \left(\frac{l_e}{\delta}\right)^{1.5} sin^{-1}\left(\frac{d_{r1}}{l_r}\right) + C_d \left(\frac{2}{5}\eta^{\frac{1}{2}}\right)^{\zeta-1} (d - d_{r1})^{2\zeta-1} & for\ d > d_{r1} \end{cases} \tag{36}$$

Simulations run for Dragon Skin 10 and Dragon Skin 30 materials conform to the model for both

regimes, as shown in Figure 28.
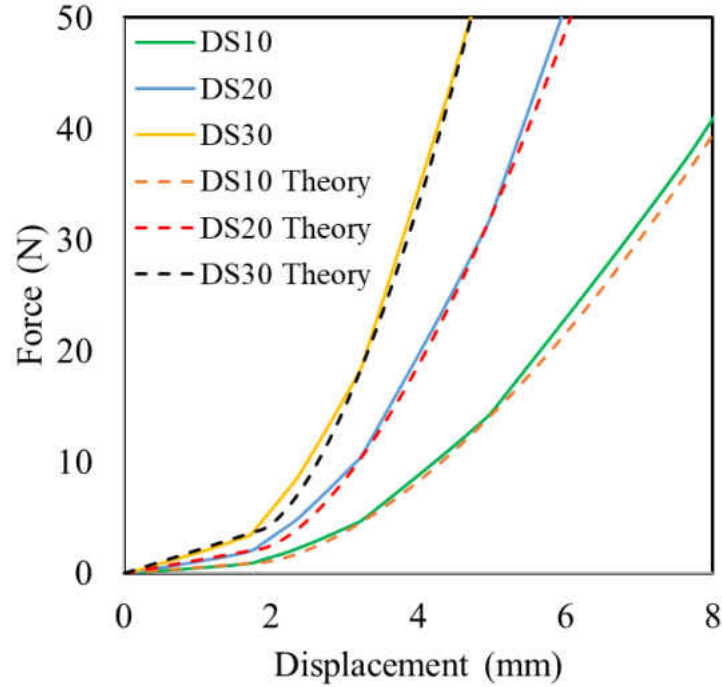
Figure 28. Full model force-displacement relation for varied material

3.5 Anisotropy of the Contact Surface

While the contact radius of the indenter is shown to be insignificant in the force-displacement response of the scaled system, it is observed to play a key role in the stress distribution through the contact surface. The contact surface shows an anisotropic distribution, with the scales to the right of the indenter coming into contact and distributing the load, and the scales to the left being pulled down by the associated deformation. There is an increasingly anisotropic response for indenters of decreasing radius, as larger indenters can come into contact with additional scales on the left, further distributing the load. For clarity, this distribution is displayed at a greater indentation depth for a nonlinear elastic material with lower stiffness, where $E = 0.19$ MPa, in Figure 29. This observed to be a size dependent response, where the ratio of indenter radius to total

scale length is significant and increasing this ratio decreases the anisotropy in the system as the indenter becomes capable of contacting additional scales.
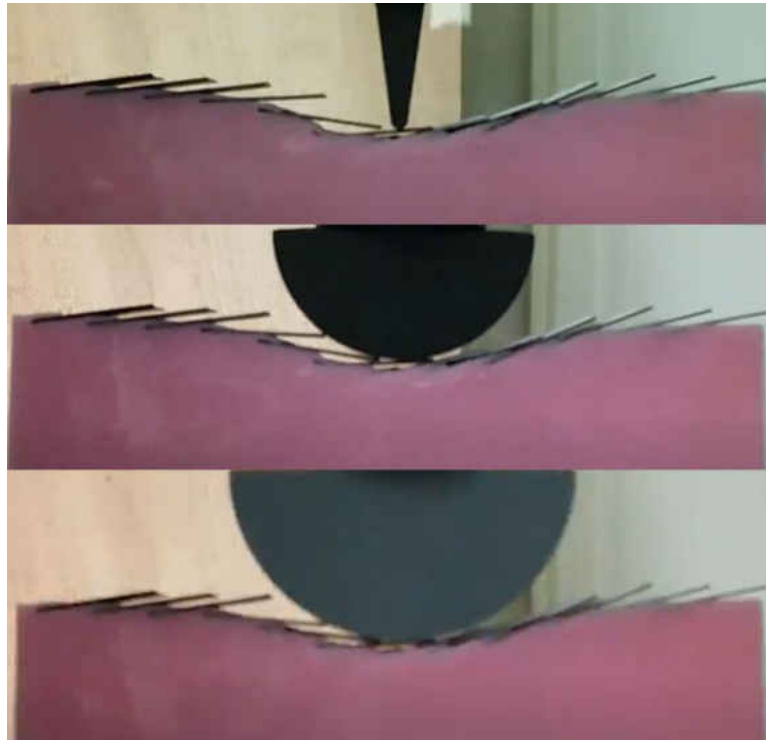
Figure 29. Contact for sample with E=0.19 MPa and η=1.6, where R=2.5, 37.5 and 50 mm

This anisotropic distribution results in the strain being concentrated to the left of the indenter and propagating from left to right, as shown in Figure 30. This response breaks the symmetry of the load across the sample and provides an avenue to draw concentrated load away from sensitive regions.

Figure 30. Load distribution for configuration with η=2.4, where R=37.5mm

CHAPTER 4: CONCLUSIONS AND FUTURE WORK

4.1 Conclusions

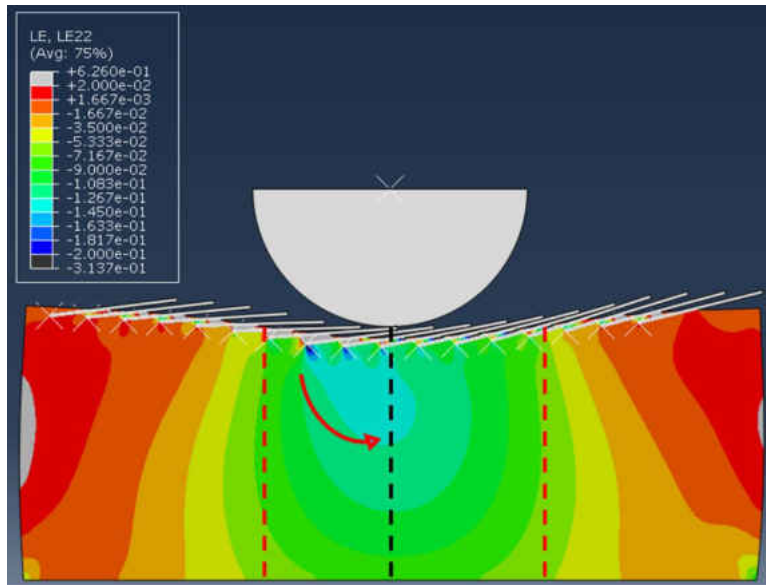From the primary and additional configurations tested it was shown that the inclusion of exoskeletal scale components greatly alters the distribution of strain across a substrate under indentation loading. This alteration is attributed to an artificial increase in the effective Hertzian contact area of the system, caused by an extension of the loading surface through the interactions of the scales. Notably, the scales are shown to trivialize the effects of indenter radius for the range of indenters tested, verifying that in the tested range the distribution of the scales is what determines the effective contact area of the system. A numerical model is developed, from the experimental and simulated data, to capture the stiffening effects resulting from the scale distribution. This model divides the scale contact into two regimes. The first regime is dominated by scale rotation, while the second regime shows the response of the full system as the substrate is deformed. The length of the first regime is approximated by the modified arc lengths of the rotating scales. The force-displacement relation of the first regime is approximated through the equation of a torsional spring. The second regime is developed from Kao's elastic model. The tunable stiffness of the second regime gives the scale structures the potential to be utilized as a mechanism for complex motion in soft robotics applications. The tunable length and stiffness of the first regime also have potential applications in areas such as collision control, providing feedback before the main body is contacted, as shown in Figure 31. Additionally, the size dependent anisotropic load distribution of the scaled system has the potential to be utilized in directing concentrated load away from sensitive regions, such as the electronic components in soft robotics applications.
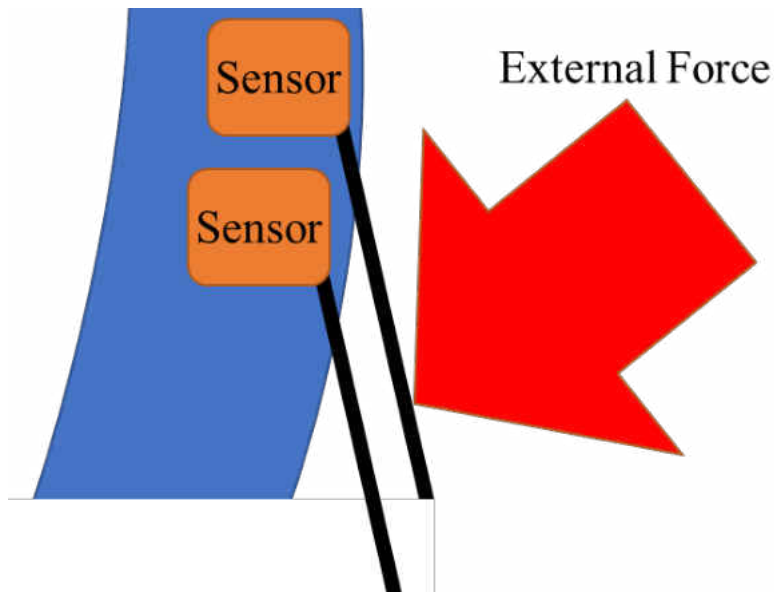
Figure 31. Applications in collision control

4.2 Future Work

Future considerations include a more thorough analysis of the response of the first regime, through the manipulation of additional parameters such as embedded scale length. Variation of the testing rate also requires further study, to quantify the observed rate dependent nonlinearity of the scaled system. The effects of the scale angle θ also require further experimental study to analyze its role in the stiffening response of the scaled system. Additionally, while it is shown that the indenter radius is not significant as it decreases in magnitude, indenters with increasing radii could significantly alter the system response by initially contacting multiple scales. To this end, there could be value in exploring the significance of the ratio of indenter radius to scale length. Further considerations could include the effects of oblique loading, and the addition of tunable parameters into the system. These could include configurations with patterns of scales with differing material properties, and the thermal tunability of scales made of metals with low melting points, such as Wood's or Field's metal.

LIST OF REFERENCES

Ali, H., Ebrahimi, H., & Ghosh, R. (2019). Bending of biomimetic scale covered beams under discrete non-periodic engagement. *International Journal of Solids and Structures*, 166, 22–31. doi: 10.1016/j.ijsolstr.2019.01.021.

Ali, H., Ebrahimi, H., & Ghosh, R. (2019). Frictional Damping from Biomimetic Scales. *Scientific Reports*, 9(1). doi: 10.1038/s41598-019-50944-0.

Ali, H., Ebrahimi, H., & Ghosh, R. (2019). Tailorable elasticity of cantilever using spatio-angular functionally graded biomimetic scales. *Mechanics of Soft Materials*, 1(1). doi: 10.1007/s42558-019-0012-2.

Ali, H., Ebrahimi, H., Stephen, J., Warren, P., & Ghosh, R. (2020). Tailorable Stiffness Lightweight Soft Robotic Materials with Architectured Exoskeleton. *AIAA Scitech 2020 Forum*, doi: 10.2514/6.2020-1551.

Autumn, K., & Gravish, N. (2008). Gecko Adhesion: Evolutionary Nanotechnology. *Philosophical Transactions of the Royal Society A: Mathematical, Physical and Engineering Sciences*, vol. 366, no. 1870, pp. 1575–1590., doi:10.1098/rsta.2007.2173.

Browning, A., Ortiz, C., & Boyce, M. C. (2013). Mechanics of Composite Elasmoid Fish Scale Assemblies and Their Bioinspired Analogues. *Journal of the Mechanical Behavior of Biomedical Materials*, vol. 19, pp. 75–86., doi:10.1016/j.jmbbm.2012.11.003.

Bruet, B. J., Song, J., Boyce, M. C., & Ortiz, C. (2008). Materials Design Principles of Ancient Fish Armour. *Nature Materials*, vol. 7, no. 9, pp. 748–756., doi:10.1038/nmat2231.

Chintapalli, R. K., Mirkhalaf, M., Dastjerdi, A. K., & Barthelat, F. (2014). Fabrication, Testing and Modeling of a New Flexible Armor Inspired from Natural Fish Scales and Osteoderms. *Bioinspiration & Biomimetics*, vol. 9, no. 3, p. 036005., doi:10.1088/1748-3182/9/3/036005.

Chowdhary, G., Mattia, G., Krishnan, G., Soman, C., & Lovell, S. (2019). Soft Robotics as an Enabling Technology for Agroforestry Practice and Research. *Sustainability*, vol. 11, no. 23, p. 6751., doi:10.3390/su11236751.

Ebrahimi, H., Ali, H., & Ghosh, R. (2020). Coulomb friction in twisting of biomimetic. *arXiv preprint arXiv:2001.11054*.

Ebrahimi, H., Ali, H., Horton, R. A., Galvez, J., Gordon, A. P., & Ghosh, R. (2019). Tailorable twisting of biomimetic scale-covered substrate. *EPL (Europhysics Letters)*, 127(2), 24002. doi: 10.1209/0295-5075/127/24002.

Ehrlich, H. (2015). Materials Design Principles of Fish Scales and Armor. In H. Ehrlich, *Biological Materials of Marine Origin Biologically-Inspired Systems* (pp. pp. 231–262). Springer.

Formlabs. (2019). *Materials Data Sheet.* Retrieved from Formlabs.com: archive-media.formlabs.com/upload/XL-DataSheet.pdf

Funk, N., Vera, M., Szewciw, L. J., Barthelat, F., Stoykovich, M. P., & Vernerey, F. J. (2015). Bioinspired Fabrication and Characterization of a Synthetic Fish Skin for the Protection of Soft Materials. *ACS Applied Materials & Interfaces*, vol. 7, no. 10, pp. 5972–5983., doi:10.1021/acsami.5b00258.

Hanlon, R. (2007). Cephalopod Dynamic Camouflage. *Current Biology*, vol. 17, no. 11, doi:10.1016/j.cub.2007.03.034.

Hao, Y., Wang, T., Ren, Z., Gong, Z., Wang, H., Yang, X., . . . Wen, L. (2017). Modeling and Experiments of a Soft Robotic Gripper in Amphibious Environments. *International Journal of Advanced Robotic Systems*, vol. 14, no. 3, , p. 172988141770714., doi:10.1177/1729881417707148.

Kao, I., & Yang, F. (2004). Stiffness and Contact Mechanics for Soft Fingers in Grasping and Manipulation. *IEEE Transactions on Robotics and Automation*, vol. 20, no. 1, pp. 132–135., doi:10.1109/tra.2003.820868.

Kim, S., Laschi, C., & Trimmer, B. (2013). Soft Robotics: a Bioinspired Evolution in Robotics. *Trends in Biotechnology*, vol. 31, no. 5, pp. 287–294., doi:10.1016/j.tibtech.2013.03.002.

Laschi, C., Mazzolai, B., & Cianchetti, M. (2016). Soft Robotics: Technologies and Systems Pushing the Boundaries of Robot Abilities. *Science Robotics*, vol. 1, no. 1, doi:10.1126/scirobotics.aah3690.

Majidi, C. (2018). Soft-Matter Engineering for Soft Robotics. *Advanced Materials Technologies*, p. 1800477., doi:10.1002/admt.201800477.

Marchese, A. D., Onal, C. D., & Rus, D. (2014). Autonomous Soft Robotic Fish Capable of Escape Maneuvers Using Fluidic Elastomer Actuators. *Soft Robotics*, vol. 1, no. 1, pp. 75–87., doi:10.1089/soro.2013.0009.

Martini, R., & Barthelat, F. (2016). Stability of Hard Plates on Soft Substrates and Application to the Design of Bioinspired Segmented Armor. *Journal of the Mechanics and Physics of Solids*, vol. 92, pp. 195–209., doi:10.1016/j.jmps.2016.04.0.

Martini, R., & Barthelat, F. (2016). Stretch-and-Release Fabrication, Testing and Optimization of a Flexible Ceramic Armor Inspired from Fish Scales. *Bioinspiration & Biomimetics*, vol. 11, no. 6, p. 066001., doi:10.1088/1748-3190/11/6/066001.

Martini, R., Balit, Y., & Barthelat, F. (2017). A Comparative Study of Bio-Inspired Protective Scales Using 3D Printing and Mechanical Testing. *Acta Biomaterialia*, vol. 55, pp. 360–372., doi:10.1016/j.actbio.2017.03.025.

Miranda, P., Pajares, A., & Meyers, M. A. (2018). Bioinspired Composite Segmented Armour: Numerical Simulations. *Journal of Materials Research and Technology*, vol. 8, no. 1, pp. 1274–1287., doi:10.1016/j.jmrt.2018.09.007.

Murcia, S. C. (2017). The Natural Armor of Fish: an Exploration of a Biological Composite. *Dissertation Abstracts International*, 79-04(E).

Pfeifer, R., Lungarella, M., & IIda, F. (2012). The Challenges Ahead for Bio-Inspired Soft Robotics. *Communications of the ACM*, vol. 55, no. 11, p. 76., doi:10.1145/2366316.2366335.

Popov, V. L. (2017). *Contact Mechanics and Friction: Physical Principles and Applications.* Springer.

Porter, M. M., Ravikumar, N., Barthelat, F., & Martini, R. (2017). 3D-Printing and Mechanics of Bio-Inspired Articulated and Multi-Material Structures. *Journal of the Mechanical*

Behavior of Biomedical Materials, vol. 73, pp. 114–126., doi:10.1016/j.jmbbm.2016.12.016.

Reichert, S. H. (2010). Reverse Engineering Nature: Design Principles for Flexible Protection. Inspired by Ancient Fish Armor of Polypteridae. *Thesis (S.M.)--Massachusetts Institute of Technology, Dept. of Architecture.*

Rudykh, S., & Boyce, M. C. (2014). Analysis of Elasmoid Fish Imbricated Layered Scale-Tissue Systems and Their Bio-Inspired Analogues at Finite Strains and Bending. *IMA Journal of Applied Mathematics*, vol. 79, no. 5, pp. 830–847., doi:10.1093/imamat/hx.

Rudykh, S., Ortiz, C., & Boyce, M. C. (2015). Flexibility and Protection by Design: Imbricated Hybrid Microstructures of Bio-Inspired Armor. *Soft Matter*, vol. 11, no. 13, pp. 2547–2554., doi:10.1039/c4sm02907k.

Siciliano, B., & Khatib, O. (2016). Contacts in Grasping and Fixture Designs. In B. Siciliano, & O. Khatib, *Springer Handbook of Robotics* (pp. 664-666). Springer.

Smooth-On, Inc. (n.d.). *Dragon Skin™ Series* . Retrieved from www.smooth-on.com: www.smooth-on.com/tb/files/DRAGON_SKIN_SERIES_TB.pdf

Trivedi, D., Rahn, C. D., Kier, W. M., & Walker, I. D. (2008). Soft Robotics: Biological Inspiration, State of the Art, and Future Research. *Applied Bionics and Biomechanics*, vol. 5, no. 3, pp. 99–117., doi:10.1080/11762320802557865.

Tsurtsumia, M. (2011). The Evolution of Splint Armour in Georgia and Byzantium: Lamellar and Scale Armour in the 10th-12th Centuries. *Byzantina Symmeikta*, vol. 21, no. 1, p. 65., doi:10.12681/byzsym.976.

Vernerey, F. J., & Barthelat, F. (2014). Skin and Scales of Teleost Fish: Simple Structure but High Performance and Multiple Functions. *Journal of the Mechanics and Physics of Solids*, vol. 68, pp. 66–76., doi:10.1016/j.jmps.2014.01.005.

Vernerey, F. J., Musiket, K., & Barthelat, F. (2013). Mechanics of Fish Skin: A Computational Approach for Bio-Inspired Flexible Composites. *International Journal of Solids and Structures*, vol. 51, no. 1, pp. 274–283., doi:10.1016/j.ijsolstr.2013.10.001.

White, Z. W. (2018). Fish-Scales: the Next Step in Soft Body Protection? *Mechanical Engineering Graduate Theses & Dissertations*, vol. 160, scholar.colorado.edu/mcen_gradetds/160.

Xydas, N., & Kao, I. (1999). Modeling of Contact Mechanics and Friction Limit Surfaces for Soft Fingers in Robotics, with Experimental Results. *The International Journal of Robotics Research*, vol. 18, no. 9, pp. 941–950., doi:10.1177/02783649922.

Zhu, D., Barthelat, F., & Vernerey, F. (2013). Intricate Multiscale Mechanical Behaviors of Natural Fish-Scale Composites. *Handbook of Micromechanics and Nanomechanics*, doi:10.1201/b14795-26.